

A targeted machine learning approach for detecting diffuse radio emission with Astronomaly: Protege

Verlon Etsebeth^{1*}, Michelle Lochner¹, Konstantinos Kolokythas^{2,3}, Kenda Knowles^{2,3}, Emma Tolley⁴

¹Department of Physics and Astronomy, University of the Western Cape, Bellville, Cape Town 7535, South Africa

²Centre for Radio Astronomy Techniques and Technologies, Department of Physics and Electronics, Rhodes University, P.O. Box 94, Makhanda 6140, South Africa

³South African Radio Astronomy Observatory, 2 Fir Street, Black River Park, Observatory 7925, South Africa

⁴Institute of Physics, Laboratory of Astrophysics, École Polytechnique Fédérale de Lausanne (EPFL), Observatoire de Sauverny, Versoix 1290, Switzerland

19 February 2026

ABSTRACT

Diffuse radio emission in galaxy clusters, such as radio halos, relics, and mini halos, is a key tracer of non-thermal processes, turbulence, and magnetic fields within the intra-cluster medium. However, their low surface brightness, as well as contamination from compact sources and imaging artefacts, makes their detection challenging. The sheer volume of data from instruments such as the Square Kilometre Array will render traditional manual-inspection based detection methods infeasible. This paper introduces a novel machine learning approach that uses active learning to rapidly identify diffuse emission candidates from a small, optimally-selected subset of data. We apply the self-supervised deep learning algorithm Bootstrap Your Own Latent to extract features from source cutouts in the MeerKAT Galaxy Cluster Legacy Survey (MGCLS). We then pass these features through the ASTRONOMALY: PROTEGE anomaly detection framework to identify the final candidates. Using a human-labelled set, we evaluate our pipeline on high-resolution ($\sim 7''$), convolved ($15''$), and combined-feature MGCLS datasets. Interestingly, the high-resolution features identify diffuse sources more efficiently than the convolved resolution, which are in turn outperformed by the combined features. Of the top 100 sources ranked by PROTEGE, 99% exhibit diffuse characteristics, with 55% confirmed as cluster-related emission. Our work shows that PROTEGE can identify diffuse emission with minimal human labelling effort, offering a powerful, scalable tool capable of detecting both known and novel diffuse radio sources.

Key words: Machine Learning – Algorithms – Radio continuum – Diffuse emission

1 INTRODUCTION

Galaxy clusters, as the largest gravitationally bound structures in the Universe, offer a valuable means of studying cosmic evolution. The intra-cluster medium (ICM) within these systems hosts a variety of thermal and non-thermal phenomena, shaped by the interplay between turbulence, magnetic fields, and particle acceleration processes (Brunetti & Jones 2014; van Weeren et al. 2019). Diffuse radio emission found within galaxy clusters originates from synchrotron radiation produced by relativistic electrons interacting with magnetic fields and trace the dynamic, non-thermal components of the ICM. They can therefore constrain theories of cosmic-ray transport and magnetic field evolution (Knowles et al. 2021). Detecting new diffuse emission structures across diverse cluster environments is therefore important for understanding the origin and physical drivers of these phenomena.

Diffuse radio *cluster* emission falls into three main classes based on morphology, location, and origin (Brunetti & Jones 2014; van Weeren et al. 2019; van Weeren et al. 2021; Hoang et al. 2022; Botteon et al. 2022; Kolokythas et al. 2025). *Radio halos* appear as megaparsec-scale emission coinciding with the centres of galaxy

clusters, overlapping with the X-ray emitting ICM, and are linked to merger-driven turbulence. *Radio relics* manifest as large, highly polarised structures at cluster peripheries and trace shock fronts from cluster mergers. *Radio mini-halos*, typically ≤ 500 kpc, occupy central regions in cool-core, dynamically relaxed clusters and arise from gas sloshing and particle re-acceleration (Giacintucci et al. 2017). Recent observations have also revealed complex structures such as radio phoenixes (revived fossil plasma) and faint emissions bridging clusters, which further contribute to understanding large-scale cosmic web formation (Cuciti et al. 2021; Venturi et al. 2022). However, diffuse emission can also occur outside of clusters from sources such as dying radio galaxies or remnant active galactic nuclei (AGN) (Osinga et al. 2021).

Modern radio facilities like LOFAR, uGMRT, and VLA have improved the detection of faint diffuse emission by offering high sensitivity and angular resolution across a range of redshifts and cluster masses (Bonafede et al. 2015; van Weeren et al. 2019; Cuciti et al. 2021). The MeerKAT Galaxy Cluster Legacy Survey (MGCLS), in particular, provided deep 1.28GHz observations with high sensitivity and resolution, ideal for studying these faint, extended structures (Knowles et al. 2022).

However, detecting these structures remains challenging due to their intrinsically low surface brightness and corresponding low

* E-mail: verlon18@gmail.com

signal-to-noise ratios (SNRs). Even with modern instruments, identifying and classifying diffuse cluster emission is complicated by contamination from compact sources such as AGN, source blending, and imaging artefacts (Kolokythas et al. 2025). Additionally, the sheer volume and complexity of data anticipated from next-generation instruments such as the SKA will render manual inspection impractical.

To address these challenges, machine learning offers scalable automation. Several approaches have emerged recently: Transformer-based segmentation models like TUNA, which uses a customised TransUNet architecture (Chen et al. 2021), employs synthetic training data to map faint extended sources in LotSS (Sanvitale et al. 2025), while multimodal foundation models such as OpenCLIP enable similarity-based searches for peculiar radio galaxy morphologies in the Evolutionary Map of the Universe (EMU) survey (Gupta et al. 2025). However, these methods require either large labelled datasets or synthetic simulations matched to the target survey, resources that may not exist for exploratory surveys where target morphologies are poorly constrained or can not be defined in advance.

Other approaches include anomaly detection, but this often identifies uninteresting outliers while burying scientifically valuable sources in complex feature spaces (Lochner & Rudnick 2024), as demonstrated by sources like SAURON being overlooked in MeerKAT data (Lochner et al. 2023). The ASTRONOMALY framework addresses this limitation by combining unsupervised anomaly detection with active learning, thereby personalising results by learning which anomalies match user preferences rather than simply flagging all outliers (Lochner & Bassett 2021).

Active learning, as implemented in ASTRONOMALY and its extension PROTEGE (Lochner & Rudnick 2024), operates differently than standard supervised machine learning. Rather than training a model on one dataset to apply to another, the algorithm works iteratively within a single dataset to identify sources of interest. There is no separate training and test split because the goal is not generalisation but rather efficient exploration of the specific dataset at hand. The algorithm continuously learns from human labels and uses this feedback to rank sources, with performance measured by how effectively interesting sources rise to the top of the ranked list. This makes PROTEGE particularly well-suited for scenarios where the targets are rare, morphologically diverse, and can not be easily defined in advance.

In this work, we combine self-supervised feature extraction using Bootstrap Your Own Latent (BYOL, Grill et al. 2020) with PROTEGE for targeted source detection. BYOL learns a compact, image-based feature representation of all sources without requiring labels, providing a structured feature space in which morphological similarities are encoded. Previous work has demonstrated that BYOL can automatically cluster galaxies with similar morphologies and highlight rare or unusual types, such as mergers (Mohale & Lochner 2024), illustrating its capability to capture meaningful features for scientific discovery. PROTEGE then operates on this feature space as a recommendation engine, guiding the search based on user-defined criteria. This enables efficient discovery of diffuse emission candidates in MGCLS data without exhaustive manual inspection. Importantly, the approach emulates exploring a completely unlabelled dataset from scratch: the algorithm makes no assumptions about what constitutes diffuse emission or its prevalence, learning these distinctions entirely from user feedback.

We aim to (1) develop and test a pipeline for detecting diffuse cluster emission in a targeted manner, (2) compare the performance of high-resolution and convolved datasets, and (3) evaluate the benefits of concatenating feature representations from different resolutions.

We describe the MGCLS data in Section 2, detail source selection in Section 3, explain BYOL feature extraction and visualisation in

Section 4, and present the ASTRONOMALY: PROTEGE implementation in Section 5. Pipeline performance is evaluated in Section 6, followed by discussion in Section 7 and conclusions in Section 8.

2 DATA

2.1 The MeerKAT Galaxy Cluster Legacy Survey

This work makes use of the MGCLS, one of the most detailed wide-field radio surveys targeting galaxy clusters (Knowles et al. 2022). MGCLS performed long-track L-band (900–1670 MHz) observations of 115 galaxy clusters, with each cluster observed for approximately 6 to 10 hours. The survey aims to study galaxy evolution, intra-cluster magnetism, cluster dynamics, star formation, and neutral hydrogen mapping in clusters.

The 64 antennas of MeerKAT, spanning 8-km with a densely packed 1-km core, provide high sensitivity images with typical RMS noise levels of $\sim 3 - 5 \mu\text{Jy beam}^{-1}$. MGCLS achieves angular resolutions ranging from approximately $\sim 7'' - 8''$ (high-resolution products) to $15''$ in convolved images, with the lower resolution considered better suited for detecting faint, extended emission. The survey is sensitive to structures up to $10'$ in angular scale.

The MGCLS also includes polarisation and spectral index image cubes, which can be used for Faraday rotation studies and mapping magnetic fields within clusters, though we do not use these products in our analysis. The basic image cubes cover a full field of view measuring $2^\circ \times 2^\circ$, allowing for wide-field observations of galaxy clusters. In contrast, the enhanced products focus on the inner $1.2^\circ \times 1.2^\circ$ field, which is corrected for the primary beam, and are used in this study.

2.2 Human Labelled Catalogue

Kolokythas et al. (2025) provides a detailed catalogue of all 115 MGCLS clusters, reporting that approximately 54% (62 of 115) display some form of diffuse radio cluster emission. This catalogue, hereafter referred to as the Human Labelled Catalogue (HLC), represents a follow-up to the original MGCLS overview (Knowles et al. 2022) and provides a detailed characterisation of diffuse structures across both high-resolution and convolved low-resolution images. The catalogue refined classifications and identified new structures, increasing the total count from 99 to 103 diffuse radio sources or candidates. Examples of catalogued sources are shown in Figure 1. This expert-labelled catalogue is used throughout this work as a benchmark to evaluate the cumulative recall performance of our pipeline and to guide labelling during the active learning phase.

2.3 Source Extraction

We performed source extraction on the MeerKAT enhanced products using the Python Blob Detection and Source Finder (PyBDSF; Mohan & Rafferty 2015), a widely used tool in radio interferometry surveys. PyBDSF identifies contiguous regions of emission, termed “islands,” and fits Gaussian components to model these sources, generating detailed catalogues and managing background noise estimation.

Radio catalogues typically use the Gaussian components to represent sources. However, to ensure diffuse emission is captured, we instead use the islands themselves to create the image cutouts used in subsequent analysis. This approach preserves extended structures

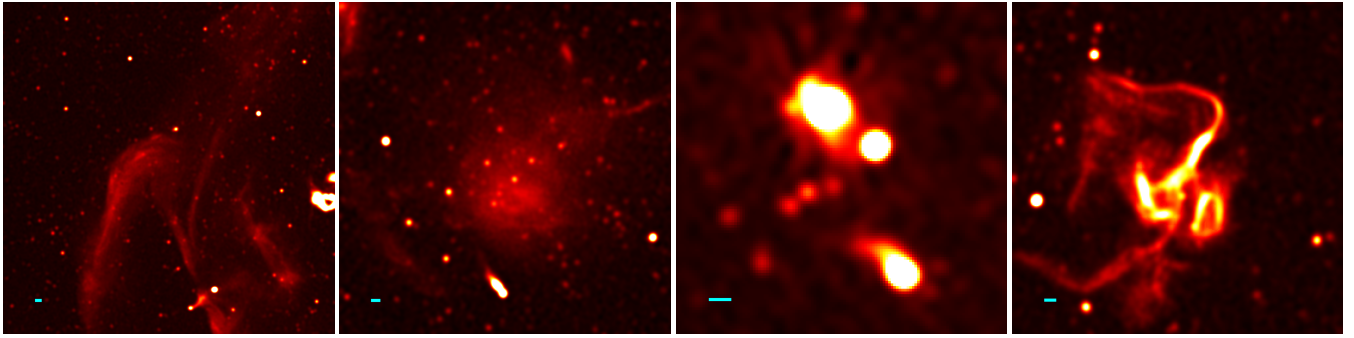


Figure 1. Examples of some of the known diffuse cluster emission in this study. From left to right: relic, halo, mini halo, and phoenix, ordered according to their frequency in the MGCLS catalogue. The beam solid angle is shown in the bottom-left corner of each cutout.

| Resolution | Source | RA (J2000) | Dec. (J2000) |
|------------|------------------|------------|--------------|
| High Res. | Abell 2811 | 00:42:08.8 | -28:32:08.8 |
| | RXC J0520.7-1328 | 05:21:02.2 | -13:35:26.5 |
| | | 05:21:09.8 | -13:29:07.7 |
| | | 05:20:49.5 | -13:31:57.0 |
| | RXC J2351.0-1954 | 23:50:41.3 | -19:56:27.1 |
| Convolved | J0027.3-5015 | 00:27:21.3 | -50:15:04.0 |
| | RXC J0520.7-1328 | 05:21:02.2 | -13:35:26.5 |

Table 1. Tracers not detected and extracted using the default parameters of PyBDSF.

that might otherwise be inadequately represented by a small number of Gaussian components.

We inspected a range of PyBDSF parameter choices, assessing their effect through the trade-off between retention of known sources from the HLC and the total number of extracted sources. As no configuration tested improved HLC source recovery without substantially increasing the resulting catalogue size within the parameters explored, we adopted the standard PyBDSF thresholds of `thresh_isl=3.0` and `thresh_pix=5.0`.

3 SOURCE SELECTION

PyBDSF source extraction on the high-resolution and convolved datasets yielded 62,587 and 40,879 cutouts respectively. Most of these sources are compact and could be filtered out to reduce computational costs. However, any filtering needs to preserve the known diffuse emission sources from the HLC (Section 2.2), as these are the primary targets of this study.

3.1 Tracers

We manually inspected each extracted cutout and visually compared it to the sources listed in Kolokythas et al. (2025) to identify matches. We refer to the matched cutouts as *tracers* throughout this work, as they allow us to assess pipeline performance. Using this procedure, we identified 128 tracers in the high-resolution dataset and 145 in the convolved dataset, exceeding the 103 sources listed in the HLC. This increase arises because a single diffuse structure can be fragmented into multiple PyBDSF islands, each producing a separate cutout.

In addition, some HLC sources were not detected using the default parameters of PyBDSF, and are shown in Table 1. Visual inspection of these undetected sources confirmed they have low signal-to-noise ratios that fall below the default detection thresholds.

The tracers serve a dual purpose in our pipeline: they act as known examples that guide the algorithm during training, and simultaneously provide the basis for evaluating performance. This emulates a real-world scenario where the true number of diffuse sources is unknown and differs from supervised learning approaches, where labelled data is separated into training and evaluation sets, or unsupervised methods, which use labels only for evaluation. The use of tracers for both guiding the algorithm and evaluating performance, along with the reasoning behind this approach, are discussed in Section 7.1.

3.2 Beam Cut Application

With the number of tracers in each dataset identified, we investigated the effect of different data cuts on the relevant dataset. Unlike Lochner & Rudnick (2024), which used PyBDSF Gaussian components as complexity proxies, we apply a beam-size based cut designed to preferentially retain spatially extended emission. This removes most of the compact sources that dominate the catalogues, focusing the analysis on diffuse structures while also reducing the overall dataset size.

Assuming a Gaussian beam, we calculate the beam solid angle as $A \approx 1.133 \times (\text{FWHM})^2$, where FWHM is the Full Width Half Maximum of the MeerKAT synthesized beam. This area is converted to pixel units and used as a reference scale. For each PyBDSF island, the measured pixel area is compared to multiples of the beam area, and sources smaller than a chosen threshold are excluded.

Figure 2 compares the Gaussian component cut, defined as a threshold on the number of Gaussian components fitted to each source as implemented in Lochner & Rudnick (2024), with our beam-size cut, plotting the number of sources and tracers remaining as a function of the applied cut. The key advantage of the beam-size cut becomes apparent when comparing tracer retention: for a similar final dataset size, the beam-size based cut retained a significantly higher number of tracers compared to the Gaussian component cut. This improvement occurs because the beam-size cut directly measures spatial extent rather than model complexity. Diffuse structures may have low Gaussian component counts if PyBDSF fits them with a few components only, causing them to be incorrectly excluded by component-based cuts. By measuring sizes relative to the beam, our approach better preserves extended emission regardless of its model representation.

We note that the selection of this threshold makes use of tracer information and therefore represents an informed choice rather than a fully blind selection. The implications of this are discussed in Section 7.1.

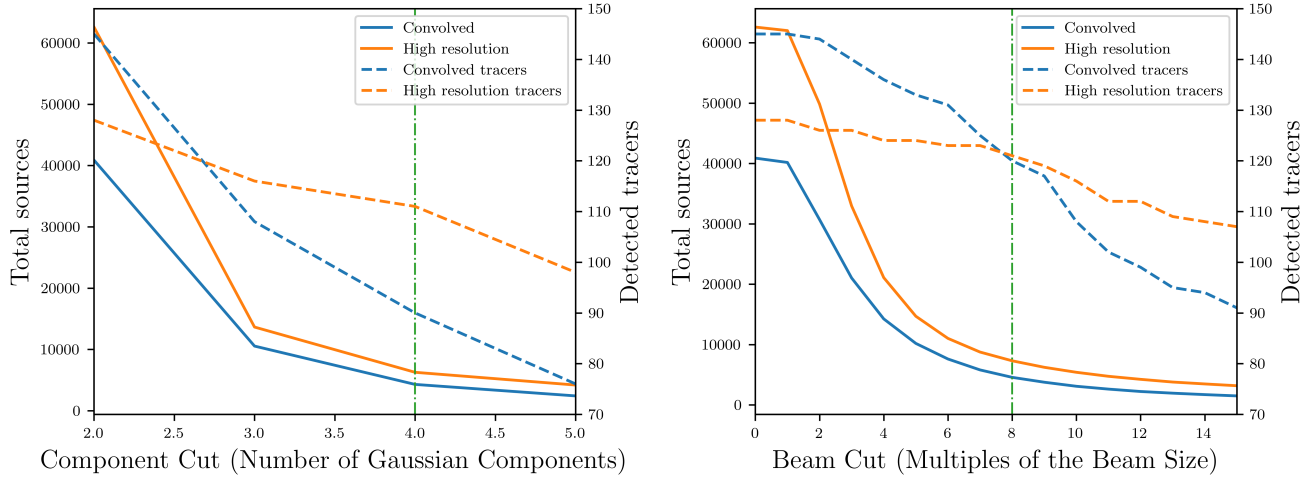


Figure 2. Comparison of data cuts applied to MGCLS sources. Left: Gaussian component-based cut from [Lochner & Rudnick \(2024\)](#). Right: Beam-size cut proposed here. Plots show the number of sources (solid lines) and tracers (dashed lines) remaining in high-resolution (orange) and convolved (blue) versus cut threshold (Gaussian components or beam-size multiples). The vertical lines mark the selected thresholds. It is evident that the beam-size cut retains more tracers for similar subset sizes.

After applying the beam-size cut, the high-resolution dataset retained 7,051 sources (121 tracers) from the initial 62,587 sources (128 tracers), and the convolved dataset retained 4,319 sources (119 tracers) from the initial 40,879 sources (145 tracers). The chosen threshold, shown as a vertical green line in [Figure 2](#), was selected to balance tracer retention with dataset size reduction. The tracers excluded by this cut are primarily compact or marginally resolved sources such as compact mini-halos. While this cut does sacrifice some completeness, it substantially reduces the dataset size while retaining the majority of the tracers that are the primary focus of this study.

4 FEATURE EXTRACTION AND VISUALISATION

Images often contain too much information for direct pattern recognition. Even a 128×128 pixel cutout represents a high-dimensional space, making it computationally expensive and statistically challenging to identify similarities between sources. We need to reduce these images into compact numerical representations that preserve morphological information relevant to diffuse emission while discarding irrelevant details like noise and background variations. We use BYOL, a self-supervised deep learning algorithm, to extract these representations automatically without requiring labelled training data.

4.1 Preprocessing

Cutouts whose bounding boxes intersect the edge of the original MGCLS field are removed, as truncated images could bias feature extraction. For each remaining PyBDSF island, we define a bounding box enlarged by a factor of 1.15 to ensure the full source is captured, and resize the resulting cutout to 128×128 pixels using `SKIMAGE` ([van der Walt et al. 2014](#)), with smaller sources interpolated using bicubic interpolation and larger sources downsampled.

Following [Lochner & Bassett \(2021\)](#), we apply sigma clipping and masking using the process implemented in `ASTRONOMALY`. Pixels outside the source contour, determined with `OPENCV`, are masked

if they lie outside a 3σ threshold, where σ is the standard deviation of the local background noise estimated from the pixel intensity distribution. This isolates genuine astronomical emission while removing background noise. For visualisation only, *asinh* scaling is applied to adjust brightness ranges without affecting the data used for feature extraction.

4.2 BYOL

Bootstrap Your Own Latent (BYOL, [Grill et al. 2020](#)) is a self-supervised learning algorithm that learns low-dimensional representations from unlabelled images. Unlike contrastive methods that require negative sample pairs, BYOL uses two neural networks, an online network and a target network, that learn from each other through an iterative prediction task. Two augmented views of the same image are generated; the online network predicts the representation of the target network of one view, while the weights of the target network are updated via a slow-moving average of the weights of the online network. This bootstrapping process allows progressive improvement without requiring labelled data or explicit negative examples.

We implement BYOL using the EfficientNet-B0 architecture ([Tan & Le 2020](#)), chosen for its balance between performance and computational efficiency. The network outputs a 1280-dimensional feature vector for each image. Following [Lochner & Rudnick \(2024\)](#), we train for 100 epochs using the Adam optimiser, with the same hyperparameter values and training setup. Training and validation loss curves ([Section A1](#)) confirm that the model learns robust representations without overfitting.

4.3 Dimensionality Reduction

To maximise performance and computational efficiency, we applied Principal Component Analysis (PCA, [Hotelling 1933](#)) to reduce the dimensionality of the BYOL feature space while retaining 95% of the variance. This reduced the representation to 37 components for the convolved data and 40 for the high-resolution data, lowering data volumes by over 97%. PCA removes redundancy by eliminating

correlated features and often improves downstream performance by reducing noise. Although it assumes linear relationships between features and may not capture all structure in the BYOL embedding space, PCA remains a widely used and effective approach in similar applications.

4.4 Visualisation

Visualising the feature space provides insight into how well the model learned meaningful representations and how different source types are organised relative to one another. However, the PCA-reduced feature space remains too high-dimensional for direct visualisation. To overcome this, we use Uniform Manifold Approximation and Projection (UMAP, McInnes et al. 2020) to embed the data into two dimensions while preserving local and global relationships between points. We implemented UMAP via the `umap-learn` Python package (Sainburg et al. 2021) with a minimum distance of 0.1 and 20 neighbours, which produced stable embeddings.

The resulting embedding places similar sources close together, enabling intuitive exploration of structure in the feature space. Due to the random nature of UMAP and the sensitivity to parameter choices, these embeddings are used for visualisation only; all quantitative analyses and evaluations are performed on the PCA-reduced features. While UMAP should not be interpreted as an exact projection, it reliably reflects genuine similarities learned by BYOL when the input features are well structured.

5 ACTIVE LEARNING WITH PROTEGE

Walmsley et al. (2022) and Lochner & Bassett (2021) demonstrated that deep features, while effective at grouping together similar sources, produce relatively uniform spaces in which rare or scientifically interesting sources are often missed by traditional anomaly detection methods. To address this, they proposed replacing anomaly scoring with a regression-based approach using Gaussian processes (Rasmussen & Williams 2006) combined with active learning. This allows users to iteratively refine searches based on their specific scientific interests rather than generic outlier metrics. This approach has been incorporated into the ASTRONOMALY framework as PROTEGE (Lochner & Rudnick 2024). We use BYOL-extracted features (Section 4.2) as input to PROTEGE to identify diffuse emission candidates.

PROTEGE operates through iterative active learning. In each iteration, the algorithm uses an acquisition function to select a batch of sources for human inspection, prioritising those that are expected to most improve its understanding of user preferences. The user labels these sources, and the algorithm updates its model to better predict which unlabelled sources match the interests of the user (see Section A2 for an illustration). This process continues until the improvement in ranking performance from additional labels becomes negligible, or until the user is satisfied with the ranked recommendations.

We adapt the implementation of PROTEGE in three ways. First, we focus exclusively on diffuse cluster emission rather than multiple anomaly types. Second, we simplify the labelling scheme: sources matching the tracers (Section 3.1) receive a score of 5, while all others receive 0 (see Figure 1). This binary approach reduces labelling inconsistency compared to the full 0-5 gradient scale. Third, we increase the batch size labelled in each iteration from 10 to 15 labels per iteration (compared to Lochner & Rudnick 2024), as preliminary tests showed 10 labels were insufficient to quickly identify the first

instances of tracers. We limit the total number of labelled sources to 300 across all iterations (20 iterations total).

The simplified labelling scheme trades flexibility for consistency. While the full gradient allows expressing degrees of interest, it introduces subjectivity in how intermediate scores are assigned. Our binary approach provides a controlled test of whether PROTEGE can learn to distinguish a specific morphological class from the general population when given clear examples.

6 RESULTS

Evaluating any non-supervised learning approach presents challenges, particularly for any dataset where the full population of targets is unknown, as is the case when exploring new data. In this work, tracers are used both to guide the iterative active learning process and to evaluate performance, where a fraction of them will have been seen by the algorithm during training. This reflects the design of PROTEGE rather than a standard supervised approach.

Our approach generates “cumulative curves” (or “cumulative anomaly curves”) that track how the tracers rank as the algorithm learns during active learning. At each iteration, PROTEGE assigns scores to all sources based on predicted “interestingness,” producing a ranked list with the most promising candidates at the top. These curves show the cumulative number of tracers recovered within the top N ranked sources, representing the reality that a user only has the capacity to inspect a limited number of sources. Steeper curves indicate faster recovery of tracers, while a diagonal curve reflects random ordering.

In practice, without a ground truth dataset, performance will be evaluated largely by a manual and visual inspection of the top N ranked candidates, such as Figure 3 where the top 100 are shown.

6.1 High Resolution versus Convolved

We analysed both MGCLS datasets separately to assess how image resolution affects detection and feature representation. Diffuse cluster emission spans multiple spatial scales, and different resolutions reveal complementary information: high-resolution imaging captures fine structural detail but can fragment or suppress faint extended emission, while convolved images enhance sensitivity to low-surface-brightness structures at the cost of fine detail. Analysing both allows us to evaluate how these differences influence feature extraction, source ranking, and overall detection performance.

Both datasets underwent preprocessing (Section 4.1), feature extraction (Section 4.2), dimensionality reduction (Section 4.3), and analysis with PROTEGE (Section 5), with binary labelling applied to tracers and non-tracers.

Figure 4 shows the cumulative anomaly curves across several labelling iterations for the different resolutions. Figure 4 shows that nearly 45% (54 of 121 for the high resolution) of the tracers can be recovered within 1% (top 100) of the subset with minimal human labelling (300 labels), highlighting the strong performance of PROTEGE in prioritising diffuse emission candidates. Significant improvements are also seen with as few as 60 labels provided (with 50% of the tracers recovered in 15% of the data), and further iterations continue to improve the rankings, although with diminishing returns. This trend matches previous findings (Etsebeth et al. 2024), where improvements plateau once sufficient examples are provided.

Comparing the two datasets, the cumulative curve for the convolved images rises to a higher value at the top of the ranked list (top 1000), suggesting better early recovery of tracers. This

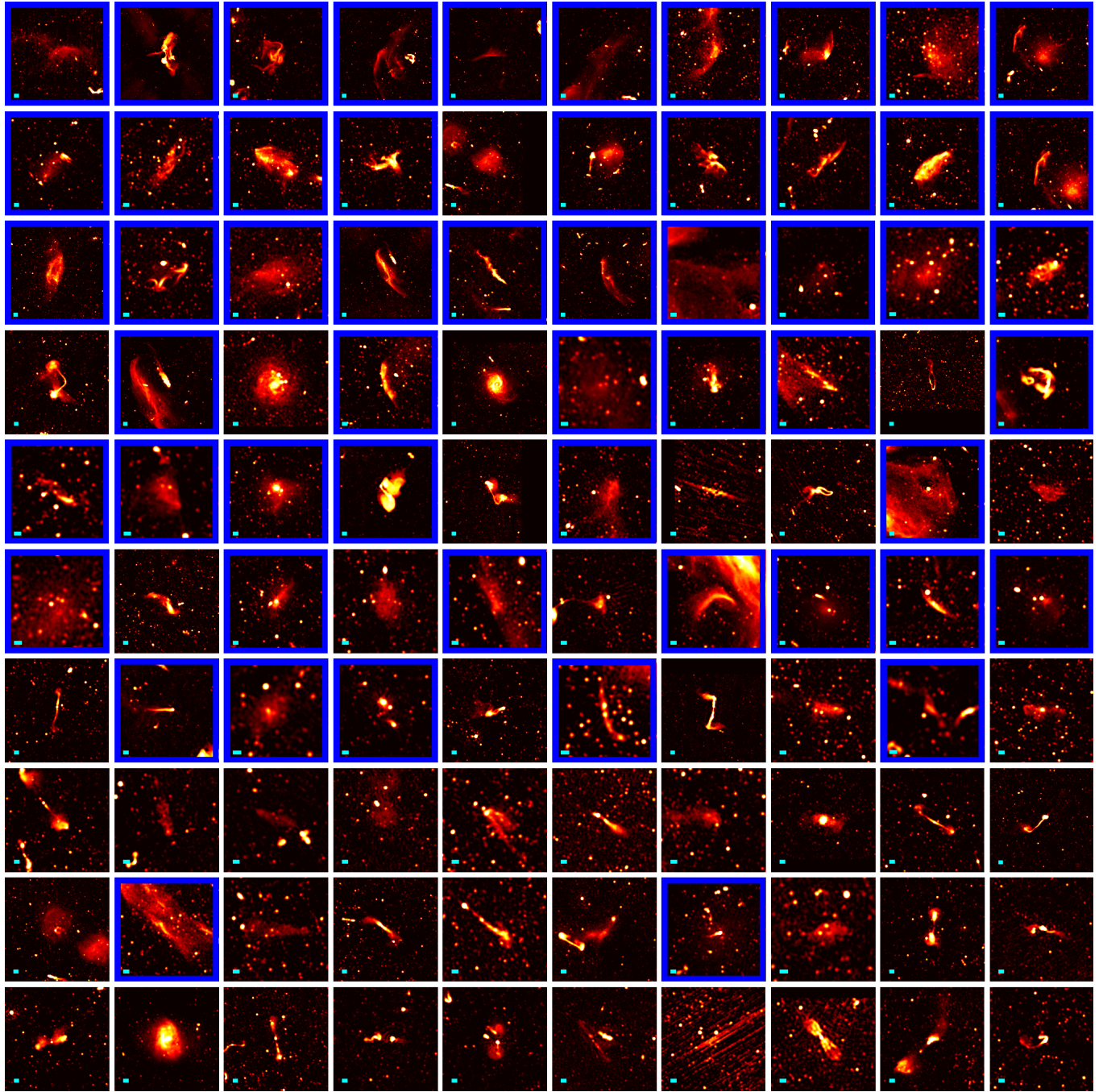


Figure 3. Top 100 ranked sources from the concatenated high-resolution subset (see Section 6.1). Known tracers are highlighted with blue frames. The beam solid angle is shown in the bottom-left corner of each cutout. 99 of the 100 sources represent some form of diffuse and/or extended radio emission, highlighting the performance of the algorithm. The other source corresponds to an artefact. A more detailed analysis of these sources is presented in Section 6.4.

likely reflects that convolved images enhance extended low-surface-brightness structures while smoothing fine-scale noise, making diffuse emission more distinguishable in the feature space. However, differences in the total number of sources between datasets, and the choice of top N sources inspected, must be taken into account before any comparison can be made. As explored in Section 6.3, examining the top 500 candidates allows a fairer comparison of pipeline performance across resolutions, mimicking a realistic scenario where only a subset of sources in a new dataset can be inspected.

Overall, both datasets demonstrate that PROTEGE efficiently priori-

tises diffuse emission candidates, with early detection and reduced human inspection workload achieved across both resolutions.

Figure 5 visualises the feature spaces of both datasets using UMAP, with tracers in red and all other sources in grey. The disjointed groupings and dispersion of tracers across the feature space reflects the diversity of the learned representations in the two datasets. This scattered distribution poses two challenges: the algorithm must learn multiple distinct morphological patterns rather than a single coherent cluster, and the isolated tracers embedded among the general population are likely to be missed, as active learning prioritises regions

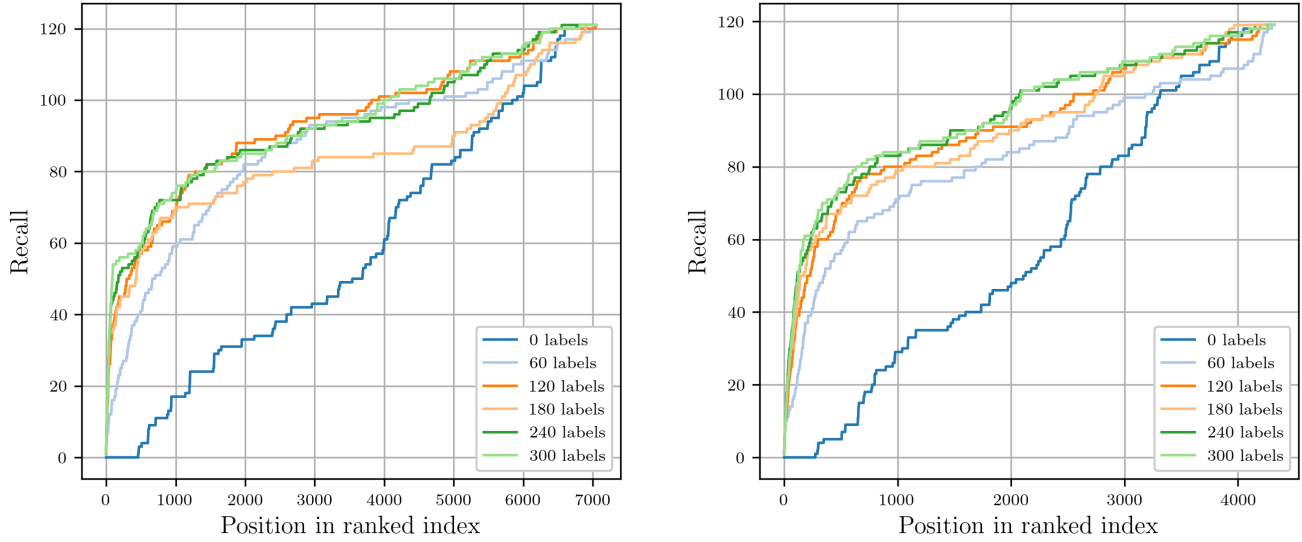


Figure 4. Cumulative anomaly curves for the high-resolution dataset (on the left with 121 tracers in total) and the convolved dataset (on the right with 119 tracers in total), showing the cumulative number of tracers recovered within the ranked list for different labelling iterations. The “0 labels” curve corresponds to the initial distribution of tracers prior to labelling. Both datasets show significant improvements in the cumulative number of tracers with iterative labelling, although diminishing returns are observed in later iterations.

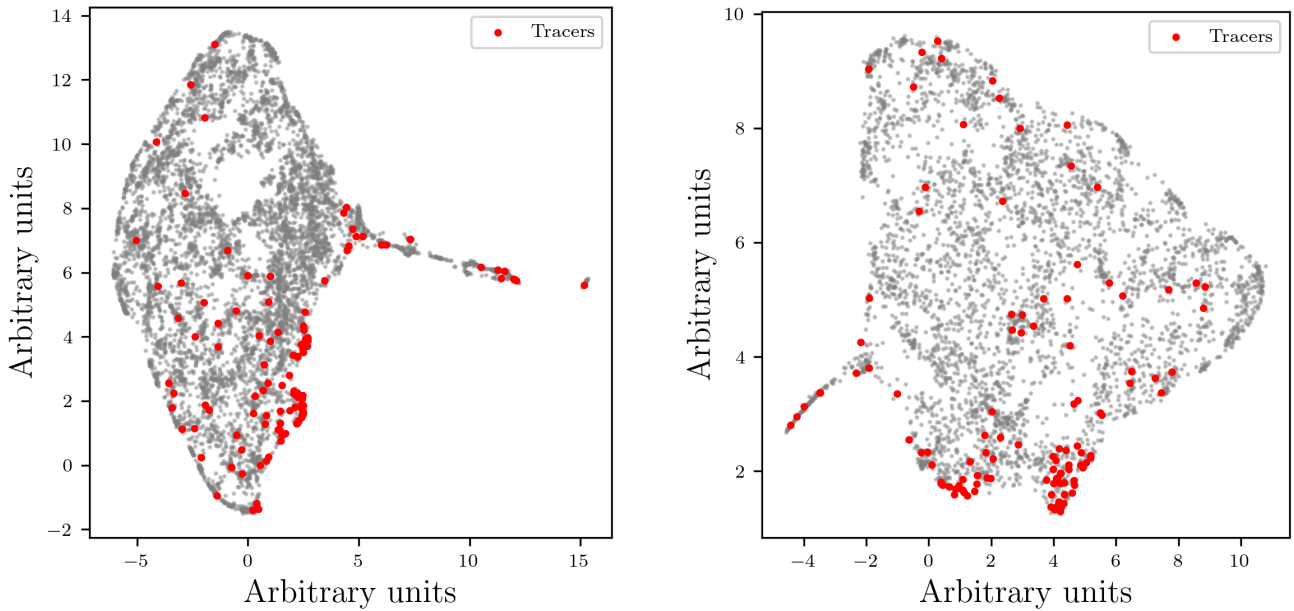


Figure 5. UMAP visualisations of the high resolution (left) and convolved (right) feature spaces. Red points indicate the tracers and grey points represent all other sources. In both cases, the tracers form several groupings with some sources dispersed across the feature space, presenting a challenge for detection with machine learning.

similar to already-labelled examples. The structure of the feature space is further discussed in Section 7.3.

6.2 Concatenated Features

As shown in Figure 6, the high-resolution and the convolved datasets exhibit different cumulative recall behaviours within the top 500

ranked sources. High-resolution features yield a steeper initial rise, suggesting that known tracers are concentrated near the top of the list. Conversely, convolved features exhibit a more gradual increase but recover a larger fraction of tracers across the full top 500. Because these behaviours are complementary, we investigated combining both resolutions into a single representation by simply concatenating the two sets of features before dimensionality reduction.

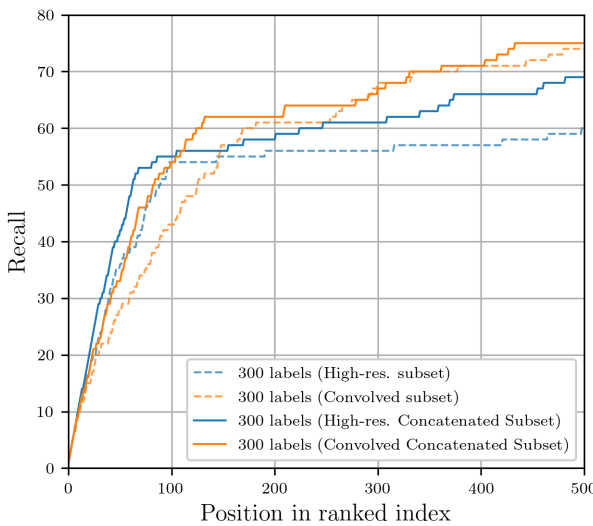


Figure 6. Cumulative curves for the top 500 sources across all configurations: standalone high-resolution and convolved datasets, plus concatenated features using either high-resolution or convolved coordinates.

To ensure consistency, we used PyBDSF island coordinates and size information to generate matching cutouts across resolutions. By applying coordinates from one dataset to images from the other, we extracted BYOL features consistently from both resolutions. Each source was thus represented by two 1280-dimensional vectors, which were concatenated into a single 2560-dimensional vector before applying PCA.

We tested two configurations: (1) using high-resolution coordinates on convolved images, and (2) using convolved coordinates on high-resolution images. Because PyBDSF identifies different numbers and extents of islands in each dataset, these configurations produce distinct source samples even for the same fields.

The cumulative recall performance of these concatenated representations (solid lines in Figure 6) was evaluated using 300 labelled sources over 20 active learning iterations, focusing on the top 500 ranked sources to emphasise early detection.

6.3 Overall Comparison

Figure 6 compares the performance of all four configurations: the standalone high-resolution and convolved features, along with the two concatenated representations. Across all configurations, high-resolution features consistently exhibit steeper initial increases in cumulative recall within the top 100 sources.

Specifically, 54 out of 121 tracers appear in the top 100 for the high-resolution features, compared to 55 for the high-resolution concatenated features. This indicates that high-resolution imaging alone is sufficient for targeted searches and rapid identification of the most morphologically distinct diffuse emission, with the addition of convolved information producing only a minor improvement in the top 100. Beyond the top 100 however, including convolved information improves overall recovery: in the top 500 sources, the high-resolution dataset alone recovers 67 out of 121 tracers, while the high-resolution concatenated representation recovers 75 out of 121.

For the convolved features, the pattern is reversed. In the top 500, the convolved dataset recovers 74 out of 119 tracers, while the convolved concatenated dataset recovers 75, showing minimal

improvement with the added high-resolution information. However, in the top 100, the convolved features recover 43 tracers, whereas the convolved concatenated features recover 54, demonstrating that the high-resolution information enhances early detection rates.

These trends reflect the complementary strengths of the two resolutions. High-resolution features excel at identifying the most prominent and morphologically distinct sources, while convolved features improve recovery of fainter, extended emission across larger scales. Concatenated representations combine these advantages, retaining early detection performance from the high-resolution features and improved overall recovery from the convolved features. Consequently, when both resolutions are available, concatenated representations enhance both early detection and overall recovery, whereas the standalone high-resolution dataset remains suitable for rapid identification of prominent sources and the standalone convolved dataset is optimal for comprehensive searches prioritising completeness.

6.4 Top 100 Investigation

We conducted a visual inspection of the top 100 ranked sources from the concatenated high-resolution coordinate subset, which recovered the most tracers within this range. Figure 3 displays these sources, with known tracers highlighted by blue frames.

The visual inspection reveals results that the cumulative plots do not reflect: 99 of the 100 top-ranked sources exhibit diffuse emission of some sort. Of these, 55 correspond to diffuse cluster emission and match the known tracers. The remaining 44 sources include radio AGN galaxies with jets and/or extended lobes, radio AGN galaxies with unusual structures (such as bent tail or wide angle tail morphologies), face-on spiral galaxies where the radio emission traces star-forming regions, and several unidentified extended structures. All display some form of diffuse radio emission, albeit produced by different physical mechanisms.

These sources exhibit diffuse radio structures and could represent potential cluster-associated emission. However, confirming this would require additional investigation, such as X-ray imaging to detect associated intra-cluster medium or spectroscopic redshifts to establish cluster membership. Some sources may instead correspond to background galaxies, diffuse emission from AGN in galaxy groups rather than cluster-associated emission, or radio galaxies with extended lobes viewed from unusual angles.

While the algorithm successfully identifies diffuse sources, distinguishing genuine cluster-associated emission from other instances requires a follow-up analysis beyond the scope of this automated detection pipeline.

6.5 Investigation of Tracers in Lower-Ranked Positions

While the ranking produced by the algorithm places most tracers near the top of the list, understanding why some rank poorly provides insight into its limitations. Figure 7 shows their distribution across the full ranked list using the concatenated high-resolution coordinate configuration. Most are concentrated within the top 1000 sources, but the distribution extends all the way down the list.

To investigate why some tracers rank poorly, we partitioned the ranked list into coloured bins (each containing 1000 sources) and examined representative sources from each. Figure 8 shows these representative tracers alongside their eight nearest neighbours in feature space (measured using Euclidean distance).

Visual inspection reveals why these sources challenge the algorithm. Most are small with low signal-to-noise ratios, leaving them

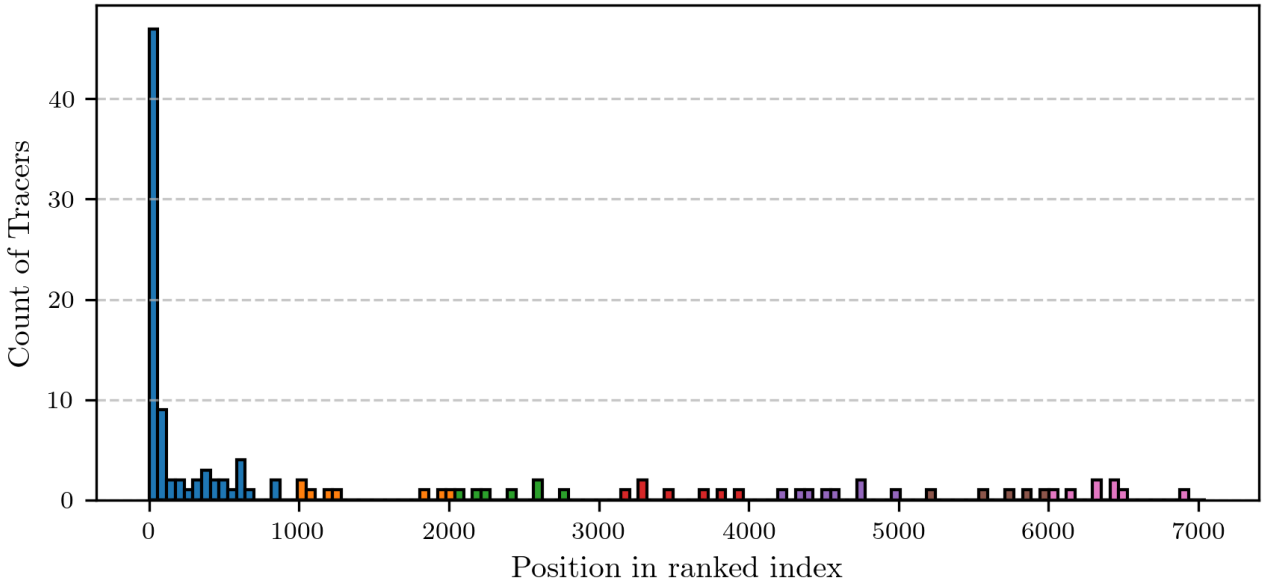


Figure 7. Histogram of tracers across the full ranked list using the concatenated high-resolution features. Bars are colour-coded in bins of 1000 sources each. Most tracers appear within the top 1000 sources, but some rank considerably lower.

with few distinctive morphological features that can be learned by BYOL. Their nearest neighbours in feature space similarly show compact or ambiguous morphologies, confirming that these tracers occupy regions dominated by non-diffuse sources.

This ambiguity is further illustrated by a candidate diffuse cluster emission source in Abell 22, shown in Figure 9. In our cutout (left panel), the emission appears faint and ambiguous, whereas the MG-CLS analysis (right panel) identifies it as a candidate diffuse radio halo (adapted from Kolokythas et al. 2025). This demonstrates how easily such sources can be overlooked without additional contextual information, such as cluster centre positions or X-ray data. This highlights an inherent limitation that is further discussed in Section 7.3: morphological diversity within the “diffuse cluster emission” category results in some examples resembling the general population more than other tracers.

Nonetheless, our pipeline with the concatenated features achieves strong overall performance. After labelling 300 sources (20 iterations of 15 labels each), 55 of the 121 tracers are detected after viewing a total of 100 sources (and half of all tracers, 61 of 121, are detected after viewing a total of 250 sources) out of the original 62,587 sources. This dramatic reduction in human effort makes the search for diffuse emission feasible in the SKA-scale era.

7 DISCUSSION

Our results demonstrate that PROTEGE can effectively identify diffuse emission in large surveys, but the methodology raises important questions about the role of labelled data, the limits of morphology-based classification, and what constitutes “successful detection” when targets are morphologically diverse. We address these questions in the following subsections.

7.1 Guiding Active Learning with Tracers and Expertise

Known diffuse cluster emission tracers are used both to guide the pipeline and to evaluate its effectiveness. For example, in defining the beam-size cut (Section 3.2), the tracers reveal how different thresholds affect the retention of extended structures. While both Gaussian component and beam-size cuts could be applied, examining the tracers allows us to choose a cut and a threshold that better preserves known diffuse emission sources.

Comparing Gaussian component and beam-size based cuts (Figure 2) highlights why this matters in practice. Some diffuse structures consist of only a few Gaussian components, which would be excluded under a component-count threshold. By contrast, a beam-size criterion, selected with guidance from tracers, remains sensitive to extended morphology regardless of the number of fitted components.

During the active learning phase, the tracers are used to train the model in a way that mimics how an expert would explore an unlabelled dataset. By labelling known examples that appear during the labelling iterations, the algorithm learns to prioritise sources with similar diffuse morphologies. This approach allows someone with less experience to label effectively, using the tracers as a reference for what an expert would consider interesting.

The tracers also provide a practical benchmark for assessing performance. By tracking how many appear cumulatively in the top N ranked sources, we can see how efficiently the pipeline recovers relevant diffuse emission for inspection. Using this combination of tracer guidance and iterative labelling, PROTEGE can identify rare or subtle sources without relying on classification approaches.

7.2 Methodological Choices

The use of PyBDSF for source extraction proved surprisingly effective when islands instead of Gaussian components are used, but has limitations for faint diffuse structures. Default parameters can miss low-SNR sources or fragment very extended emission into multiple

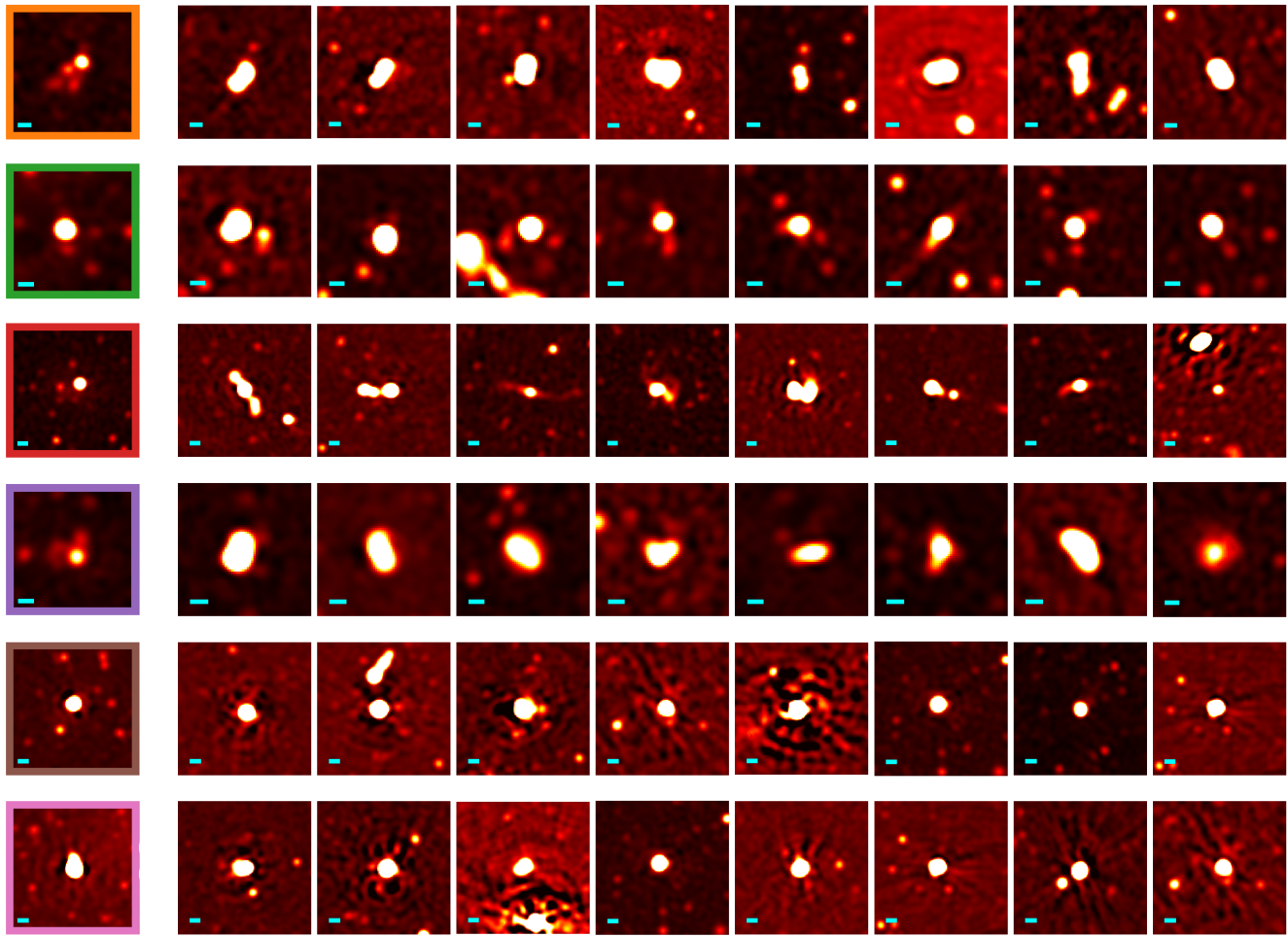


Figure 8. Tracers selected from throughout the ranked list (coloured frames matching the bins in Figure 7), shown with their eight nearest neighbours in feature space. These low-ranked sources are typically faint, compact, or barely resolved, with morphologies that resemble the general population of compact sources, making them difficult to identify during active learning.

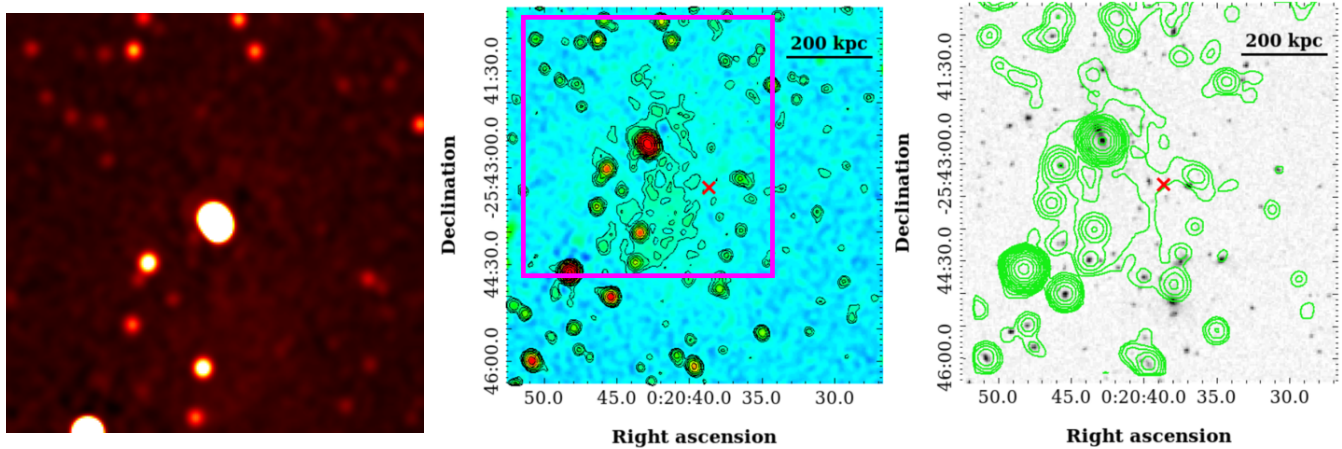


Figure 9. Diffuse radio emission associated with the galaxy cluster Abell 22. On the left: the candidate radio halo cutout created using our processing pipeline. On the middle and right: the MGCLS radio and optical view of Abell 22 adapted from [Kolokythas et al. \(2025\)](#), showing full-resolution (middle) and low-resolution (right) 1.28 GHz radio contours overlaid on optical imaging. The pink overlaid box on the middle panel indicates the region shown in our cutout on the left.

components. While fragmentation alone does not prevent detection, as each fragment can still rank highly if it displays diffuse characteristics, it does affect how the structures are represented and can complicate the interpretation of the results. A single radio halo fragmented into three PyBDSF islands might appear as three separate candidates in the ranked list rather than one coherent structure. Alternative source extraction tools or carefully tuned parameters may also improve completeness for faint emission in future applications, although this would require survey-specific optimisation.

We used a binary labelling scheme, scoring tracers as 5 and all other sources as 0, rather than the 0 to 5 gradient used in previous PROTEGE applications. While this simplifies labelling and reduces user bias, it limits the algorithm because no gradient exists to guide learning from ambiguous cases. For real-world exploration tasks, a gradient-based approach, marking clearly interesting sources as 5, ambiguous candidates as 2 to 3, and uninteresting sources as 0, would provide a stronger and more generalisable learning signal for Gaussian Processes.

7.3 Feature Space Structure

The UMAP projections of the high-resolution and convolved feature spaces (see Figure 5) show that tracers form multiple distinct groupings, with some sources dispersed throughout the embedding. This distribution reflects the morphological diversity of the tracer population, which includes both compact or barely resolved sources and highly extended emission.

Because the tracers occupy separate regions in feature space, active learning must explore multiple areas to recover all known sources. Tracers embedded among the general population are particularly challenging, as the algorithm prioritises regions similar to previously labelled examples. This scattered distribution helps explain the presence of lower-ranked sources and why some of the cumulative plots plateau. Morphologically distinct tracers that appear as outliers in the embedding are less likely to be identified based solely on similarity to previously labelled examples. This effect is particularly evident in the “180 labels” iteration of the high-resolution dataset, where cumulative recall temporarily decreases compared to “120 labels.”

This likely reflects how the Gaussian process in PROTEGE samples the feature space: if many labels come from a single cluster, the algorithm may overestimate the importance of that region and reduce sampling elsewhere, temporarily under-representing interesting sources. As further iterations rebalance sampling, the cumulative recall recovers. This emphasises the importance of maintaining a balanced selection of labelled examples during the active learning process.

7.4 Diffuse Emission versus Cluster-Associated Emission

An important distinction emerges from our results: the algorithm successfully identifies diffuse radio emission in *general*, not exclusively cluster-associated diffuse emission. Of the top 100 ranked sources, 55 are confirmed cluster-related diffuse emission (the tracers), while 44 are other forms of diffuse emission including radio AGN with jets and lobes, bent-tail and wide-angle-tail radio galaxies, face-on spirals with star-forming regions, and unidentified extended structures.

This outcome reflects a fundamental limitation of morphology-based classification using only radio imaging: distinguishing cluster-associated diffuse emission from other extended structures requires additional contextual information beyond what BYOL features can

capture. The catalogue by [Kolokythas et al. \(2025\)](#) identifies cluster emission by incorporating multiple pieces of evidence including cluster centre positions, X-ray data indicating the presence of hot ICM, spectroscopic redshifts establishing cluster membership, and the spatial correlation between radio emission and cluster properties. Our pipeline, using only radio morphology-based information, does not include this contextual information.

We therefore view the 44 non-tracer sources not as failures (or false positives) but as successes in identifying candidates worthy of follow-up investigation. Each represents a genuine detection of extended emission that could be of interest. Some may prove to be cluster-associated emission not included in the reference catalogue (either new detections or structures that were ambiguous in the original classification). Others may be interesting for different reasons, such as unusual radio galaxy morphologies, which often indicate environmental interactions or evolutionary stages worthy of study.

This distinction has important implications for interpreting the performance metrics used. The cumulative curves were calculated using the tracers only, reflecting the ability of the algorithm to recover these sources. However, the top 100 ranked candidates include both cluster-associated and non-cluster diffuse sources. As a result, the cumulative recall may underestimate the effectiveness of the algorithm in highlighting promising diffuse emission, as the top-ranked sources may contain genuine cluster emission alongside other interesting diffuse phenomena. Expert validation or multi-wavelength follow-up is therefore required to confirm the nature of these candidates.

What “successful detection” means in this study is therefore subjective: PROTEGE excels at prioritising diffuse morphologies broadly even when trained on cluster-related emission only, accelerating the discovery of rare and morphologically diverse sources, but does not perform definitive classification of cluster emission. Future work could integrate complementary information, such as redshifts, cluster membership, multiple radio frequencies for spectral information, or optical and X-ray data, to refine the prioritisation towards genuine cluster-associated emission, as highlighted in [Kolokythas et al. \(2025\)](#). By explicitly acknowledging these limitations, we can better interpret the performance metrics and guide follow-up investigations effectively.

8 CONCLUSIONS

The detection of diffuse emission in galaxy clusters remains a challenge in modern radio astronomy, particularly as data volumes continue to grow with new instruments. Our study demonstrates that combining self-supervised feature learning (BYOL) with active learning (ASTRONOMALY: PROTEGE) provides an effective approach for identifying diffuse radio emission in large astronomical datasets. Applied to the MGCLS, our pipeline substantially reduces inspection effort while recovering the majority of known diffuse cluster emission and identifies additional diffuse candidates.

Three key findings emerge from this work:

First, active learning proves well-suited for rare, morphologically diverse phenomena where traditional supervised approaches struggle due to limited labelled data. By operating iteratively within a single dataset rather than training for generalisation, PROTEGE efficiently adapts to user-defined scientific interests through minimal human feedback (300 labels across 20 iterations).

Second, resolution-dependent features capture complementary information. High-resolution imaging enables the rapid identification of prominent structures, while convolved images enhance sensitivity to faint extended emission. Concatenating features from both

resolutions combines these strengths, suggesting that multi-modal approaches incorporating additional wavelengths (X-ray, optical) or radio frequencies could further improve performance.

Third, morphology-based classification using radio imaging alone can not reliably distinguish cluster-associated diffuse emission from other extended structures (radio galaxies or star-forming regions for example). This fundamental limitation highlights the need for incorporating contextual information such as cluster positions, X-ray data, or spectroscopic redshifts, to refine candidate classifications, particularly for large-scale surveys where the manual validation of all candidates becomes impractical.

Several directions warrant future investigation. Gradient-based labelling schemes (0-5 scale) would better capture ambiguous cases than our binary approach, potentially improving sensitivity to morphological edge cases. Transfer learning experiments could test whether BYOL features trained on MGCLS generalise to other surveys or require retraining for different frequencies and resolutions. Hybrid approaches combining our method for initial candidate identification with supervised models for detailed classification could incorporate the strengths of both paradigms.

As radio surveys scale toward SKA data volumes, methods that balance automation with human expertise will become essential. Our demonstration that self-supervised learning combined with targeted active learning can efficiently identify rare phenomena provides a foundation for addressing these challenges.

Our approach excels for exploratory science targeting rare, poorly-defined morphologies, precisely where supervised methods struggle due to lack of well-defined training data.

ACKNOWLEDGEMENTS

ML, VE and Kenda Knowles acknowledges support from the South African Radio Astronomy Observatory and the National Research Foundation (NRF) towards this research. Opinions expressed and conclusions arrived at, are those of the authors and are not necessarily to be attributed to the NRF. This research made use of data from the MeerKAT telescope, a South African Radio Astronomy Observatory (SARAO) facility. SARAO is a facility of the National Research Foundation, an agency of the Department of Science and Innovation. We acknowledge use of the Inter-University Institute for Data Intensive Astronomy (IDIA) data intensive research cloud for data processing and storage. IDIA is a partnership of the University of Cape Town, the University of Pretoria, and the University of the Western Cape.

ET acknowledges support from the Swiss National Science Foundation under the SNSF Starting Grant “Deep Waves” (218396) and travel and collaboration support from the SNSF Weave/Lead Agency Grant “RadioClusters” (214815).

This work made use of the following software packages: Astronomaly (Lochner & Bassett 2021), PyBDSF (Mohan & Rafferty 2015), scikit-image (van der Walt et al. 2014), scikit-learn (Pedregosa et al. 2011), umap-learn (McInnes et al. 2020), PyTorch (Paszke et al. 2019), NumPy (Harris et al. 2020), Matplotlib (Hunter 2007), and Astropy (Astropy Collaboration et al. 2013, 2018).

DATA AVAILABILITY

The MeerKAT Galaxy Cluster Legacy Survey data used in this study are publicly available through the SARAO archive at <https://archive.sarao.ac.za>. The reference catalogue of diffuse radio

emission is published in Kolokythas et al. (2025). The Astronomaly framework and Protege extension are open-source and available at <https://github.com/MichelleLochner/astromomaly>.

REFERENCES

Astropy Collaboration, Robitaille, T. P., Tollerud, E. J., Greenfield, P., Droettboom, M., Bray, E., Aldcroft, T., Davis, M., Ginsburg, A., Price-Whelan, A. M., Kerzendorf, W. E., Conley, A., Crighton, N., Barbary, K., Muna, D., Ferguson, H., Grollier, F., Parikh, M. M., Nair, P. H., Unther, H. M., Deil, C., Woillez, J., Conseil, S., Kramer, R., Turner, J. E. H., Singer, L., Fox, R., Weaver, B. A., Zabalza, V., Edwards, Z. I., Azalee Bostroem, K., Burke, D. J., Casey, A. R., Crawford, S. M., Dencheva, N., Ely, J., Jenness, T., Labrie, K., Lim, P. L., Pierfederici, F., Pontzen, A., Ptak, A., Refsdal, B., Servillat, M., & Streicher, O., 2013. Astropy: A community Python package for astronomy, *A&A*, **558**, A33.

Astropy Collaboration, Price-Whelan, A. M., Sipőcz, B. M., Günther, H. M., Lim, P. L., Crawford, S. M., Conseil, S., Shupe, D. L., Craig, M. W., Dencheva, N., Ginsburg, A., VanderPlas, J. T., Bradley, L. D., Pérez-Suárez, D., de Val-Borro, M., Aldcroft, T. L., Cruz, K. L., Robitaille, T. P., Tollerud, E. J., Ardelean, C., Babej, T., Bach, Y. P., Bachetti, M., Bakanov, A. V., Bamford, S. P., Barentsen, G., Barmby, P., Baumbach, A., Berry, K. L., Biscani, F., Boquien, M., Bostroem, K. A., Bouma, L. G., Brammer, G. B., Bray, E. M., Breytenbach, H., Buddelmeijer, H., Burke, D. J., Calderone, G., Cano Rodríguez, J. L., Cara, M., Cardoso, J. V. M., Cheedella, S., Copin, Y., Corrales, L., Crichton, D., D’Avella, D., Deil, C., Depagne, É., Dietrich, J. P., Donath, A., Droettboom, M., Earl, N., Erben, T., Fabbro, S., Ferreira, L. A., Finethy, T., Fox, R. T., Garrison, L. H., Gibbons, S. L. J., Goldstein, D. A., Gommers, R., Greco, J. P., Greenfield, P., Groener, A. M., Grollier, F., Hagen, A., Hirst, P., Homeier, D., Horton, A. J., Hosseinzadeh, G., Hu, L., Hunkeler, J. S., Ivezić, Ž., Jain, A., Jenness, T., Kanarek, G., Kendrew, S., Kern, N. S., Kerzendorf, W. E., Khvalko, A., King, J., Kirkby, D., Kulkarni, A. M., Kumar, A., Lee, A., Lenz, D., Littlefair, S. P., Ma, Z., Macleod, D. M., Mastropietro, M., McCully, C., Montagnac, S., Morris, B. M., Mueller, M., Mumford, S. J., Muna, D., Murphy, N. A., Nelson, S., Nguyen, G. H., Ninan, J. P., Nöthe, M., Ogaz, S., Oh, S., Parejko, J. K., Parley, N., Pascual, S., Patil, R., Patil, A. A., Plunkett, A. L., Prochaska, J. X., Rastogi, T., Reddy Janga, V., Sabater, J., Sakurikar, P., Seifert, M., Sherbert, L. E., Sherwood-Taylor, H., Shih, A. Y., Sick, J., Silbiger, M. T., Singanamalla, S., Singer, L. P., Sladen, P. H., Sooley, K. A., Sornarajah, S., Streicher, O., Teuben, P., Thomas, S. W., Tremblay, G. R., Turner, J. E. H., Terrón, V., van Kerkwijk, M. H., de la Vega, A., Watkins, L. L., Weaver, B. A., Whitmore, J. B., Woillez, J., Zabalza, V., & Astropy Contributors, 2018. The Astropy Project: Building an Open-science Project and Status of the v2.0 Core Package, *AJ*, **156**(3), 123.

Bonafede, A., Intema, H., Cassano, R., Feretti, L., Giovannini, G., Govoni, F., Murgia, M., & Brunetti, G., 2015. Radio haloes in sunyaev-zel’dovich-selected clusters of galaxies, *MNRAS*, **454**(4), 3391–3404.

Botteon, A., Shimwell, T. W., Cassano, R., Cuciti, V., Zhang, X., Bruno, L., Camillini, L., Natale, R., Jones, A., Gastaldello, F., Simionescu, A., Rossetti, M., Akamatsu, H., van Weeren, R. J., Brunetti, G., Brüggen, M., Groeneveld, C., Hoang, D. N., Hardcastle, M. J., Ignesti, A., Di Gennaro, G., Bonafede, A., Drabent, A., Röttgering, H. J. A., Hoeft, M., & de Gasperin, F., 2022. The Planck clusters in the LOFAR sky. I. LoTSS-DR2: New detections and sample overview, *A&A*, **660**, A78.

Brunetti, G. & Jones, T. W., 2014. Cosmic Rays in Galaxy Clusters and Their Nonthermal Emission, *International Journal of Modern Physics D*, **23**(4), 1430007–98.

Chen, J., Lu, Y., Yu, Q., Luo, X., Adeli, E., Wang, Y., Lu, L., Yuille, A. L., & Zhou, Y., 2021. Transunet: Transformers make strong encoders for medical image segmentation.

Cuciti, V., Cassano, R., Brunetti, G., Dallacasa, D., van Weeren, R. J., Giacintucci, S., Bonafede, A., de Gasperin, F., Ettori, S., Kale, R., Pratt, G. W., & Venturi, T., 2021. Radio halos in a mass-selected sample of 75 galaxy clusters. I. Sample selection and data analysis, *A&A*, **647**, A50.

Etsebeth, V., Lochner, M., Walmsley, M., & Grespan, M., 2024. Astronomaly at scale: searching for anomalies amongst 4 million galaxies, *MNRAS*, **529**(1), 732–747.

Giacintucci, S., Markevitch, M., Cassano, R., Venturi, T., Clarke, T. E., & Brunetti, G., 2017. Occurrence of radio minihalos in a mass-limited sample of galaxy clusters, *The Astrophysical Journal*, **841**(2), 71.

Grill, J.-B., Strub, F., Altché, F., Tallec, C., Richemond, P. H., Buchatskaya, E., Doersch, C., Pires, B. A., Guo, Z. D., Azar, M. G., Piot, B., Kavukcuoglu, K., Munos, R., & Valko, M., 2020. Bootstrap your own latent: A new approach to self-supervised learning.

Gupta, N., Hayder, Z., Huynh, M., Norris, R. P., Petersson, L., Hopkins, A. M., Riggi, S., Koribalski, B. S., & Filipović, M. D., 2025. Emuse: Evolutionary map of the universe search engine.

Harris, C. R., Millman, K. J., van der Walt, S. J., Gommers, R., Virtanen, P., Cournapeau, D., Wieser, E., Taylor, J., Berg, S., Smith, N. J., Kern, R., Picus, M., Hoyer, S., van Kerkwijk, M. H., Brett, M., Haldane, A., del Río, J. F., Wiebe, M., Peterson, P., Gérard-Marchant, P., Sheppard, K., Reddy, T., Weckesser, W., Abbasi, H., Gohlke, C., & Oliphant, T. E., 2020. Array programming with numpy, *Nature*, **585**(7825), 357–362.

Hoang, D. N., Brüggen, M., Botteon, A., Shimwell, T. W., Zhang, X., Bonafede, A., Bruno, L., Bonnassieux, E., Cassano, R., Cuciti, V., Drabent, A., de Gasperin, F., Gastaldello, F., Di Gennaro, G., Hoeft, M., Jones, A., Pignataro, G. V., Röttgering, H. J. A., Simionescu, A., & van Weeren, R. J., 2022. Diffuse radio emission from non-Planck galaxy clusters in the LoTSS-DR2 fields, *A&A*, **665**, A60.

Hotelling, H., 1933. Analysis of a complex of statistical variables into principal components, *Journal of Educational Psychology*, **24**(6), 417–441.

Hunter, J. D., 2007. Matplotlib: A 2D Graphics Environment, *Computing in Science and Engineering*, **9**(3), 90–95.

Knowles, K., Pillay, D. S., Amodeo, S., Baker, A. J., Basu, K., Crichton, D., de Gasperin, F., Devlin, M., Ferrari, C., Hilton, M., Huffenberger, K. M., Hughes, J. P., Koopman, B. J., Moodley, K., Mroczkowski, T., Naess, S., Nati, F., Newburgh, L. B., Oozeer, N., Page, L., Partridge, B., Pfrommer, C., Salatino, M., Schillaci, A., Sifón, C., Smirnov, O., Sikhosana, S. P., Wollack, E. J., & Xu, Z., 2021. Merghers pilot: Meerkat discovery of diffuse emission in nine massive sunyaev-zel'dovich-selected galaxy clusters from act, *MNRAS*.

Knowles, K., Cotton, W. D., Rudnick, L., Camilo, F., Goedhart, S., Deane, R., Ramatsoku, M., Bietenholz, M. F., Brüggen, M., Button, C., Chen, H., Chibueze, J. O., Clarke, T. E., de Gasperin, F., Ianjamasimanana, R., Józsa, G. I. G., Hilton, M., Kesebonye, K. C., Kolokythas, K., Kraan-Korteweg, R. C., Lawrie, G., Lochner, M., Loubser, S. I., Marchegiani, P., Mhlahlo, N., Moodley, K., Murphy, E., Namumba, B., Oozeer, N., Parekh, V., Pillay, D. S., Passmoor, S. S., Ramaila, A. J. T., Ranchod, S., Retana-Montenegro, E., Sebokolodi, L., Sikhosana, S. P., Smirnov, O., Thorat, K., Venturi, T., Abbott, T. D., Adam, R. M., Adams, G., Aldera, M. A., Bauermeister, E. F., Bennett, T. G. H., Bode, W. A., Botha, D. H., Botha, A. G., Brederode, L. R. S., Buchner, S., Burger, J. P., Cheetham, T., de Villiers, D. I. L., Dikgale-Mahlakoana, M. A., du Toit, L. J., Esterhuysse, S. W. P., Fadana, G., Fanaroff, B. L., Fataar, S., Foley, A. R., Fourie, D. J., Frank, B. S., Gamatham, R. R. G., Gatsi, T. G., Geyer, M., Gouws, M., Gumede, S. C., Heywood, I., Hlakola, M. J., Hokwana, A., Hoosen, S. W., Horn, D. M., Horrell, J. M. G., Hugo, B. V., Isaacson, A. R., Jonas, J. L., Jordaan, J. D. B., Joubert, A. F., Julie, R. P. M., Kapp, F. B., Kasper, V. A., Kenyon, J. S., Kotzé, P. P. A., Kotze, A. G., Kriek, N., Kriel, H., Krishnan, V. K., Kusel, T. W., Legodi, L. S., Lehmensiek, R., Liebenberg, D., Lord, R. T., Lunsky, B. M., Madisa, K., Magnus, L. G., Main, J. P. L., Makhaba, A., Makhathini, S., Malan, J. A., Manley, J. R., Marais, S. J., Maree, M. D. J., Martens, A., Mauch, T., McAlpine, K., Merry, B. C., Millenaar, R. P., Mokone, O. J., Monama, T. E., Mphego, M. C., New, W. S., Ngcbeletha, B., Ngoasheng, K. J., Ockards, M. T., Otto, A. J., Patel, A. A., Peens-Hough, A., Perkins, S. J., Ramanujam, N. M., Ramudzuli, Z. R., Ratcliffe, S. M., Renil, R., Robyntjies, A., Rust, A. N., Salie, S., Sambu, N., Schollar, C. T. G., Schwardt, L. C., Schwartz, R. L., Serylak, M., Siebirts, R., Sirothia, S. K., Slabber, M., Sofeya, L., Taljaard, B., Tasse, C., Tiplady, A. J., Toruvanda, O., Twum, S. N., van Balla, T. J., van der Byl, A., van der Merwe, C., van Dyk, C. L., Van Tonder, V., Van Wyk, R., Venter, A. J., Venter, M., Welz, M. G., Williams, L. P., & Xaia, B., 2022. The MeerKAT Galaxy Cluster Legacy Survey. I. Survey Overview and Highlights, *A&A*, **657**, A56.

Kolokythas, K., Venturi, T., Knowles, K., Brüggen, M., de Gasperin, F., Sikhosana, S. P., Clarke, T. E., Smirnov, O., Loubser, S. I., & Moodley, K., 2025. The MeerKAT Galaxy Cluster Legacy Survey – II. Catalogue of the diffuse radio emission in MeerKAT-GCLS clusters, *MNRAS*, **543**(2), 1638–1704.

Lochner, M. & Bassett, B., 2021. Astronomaly: Personalised active anomaly detection in astronomical data, *Astronomy and Computing*, **36**, 100481.

Lochner, M. & Rudnick, L., 2024. Astronomaly protege: Discovery through human-machine collaboration.

Lochner, M., Rudnick, L., Heywood, I., Knowles, K., & Shabala, S. S., 2023. A unique, ring-like radio source with quadrilateral structure detected with machine learning, *MNRAS*, **520**(1), 1439–1446.

McInnes, L., Healy, J., & Melville, J., 2020. Umap: Uniform manifold approximation and projection for dimension reduction.

Mohale, K. & Lochner, M., 2024. Enabling unsupervised discovery in astronomical images through self-supervised representations, *MNRAS*, **530**(1), 1274–1295.

Mohan, N. & Rafferty, D., 2015. PyBDSF: Python Blob Detection and Source Finder, *Astrophysics Source Code Library*, record ascl:1502.007.

Osinga, E., van Weeren, R. J., Boxelaar, J. M., Brunetti, G., Botteon, A., Brüggen, M., Shimwell, T. W., Bonafede, A., Best, P. N., Bonato, M., Cassano, R., Gastaldello, F., di Gennaro, G., Hardcastle, M. J., Mandal, S., Rossetti, M., Röttgering, H. J. A., Sabater, J., & Tasse, C., 2021. Diffuse radio emission from galaxy clusters in the LOFAR Two-metre Sky Survey Deep Fields, *A&A*, **648**, A11.

Paszke, A., Gross, S., Massa, F., Lerer, A., Bradbury, J., Chanan, G., Killeen, T., Lin, Z., Gimelshein, N., Antiga, L., Desmaison, A., Kopf, A., Yang, E., DeVito, Z., Raison, M., Tejani, A., Chilamkurthy, S., Steiner, B., Fang, L., Bai, J., & Chintala, S., 2019. Pytorch: An imperative style, high-performance deep learning library, in *Advances in Neural Information Processing Systems*, vol. 32. Curran Associates, Inc.

Pedregosa, F., Varoquaux, G., Gramfort, A., Michel, V., Thirion, B., Grisel, O., Blondel, M., Prettenhofer, P., Weiss, R., Dubourg, V., Vanderplas, J., Passos, A., Cournapeau, D., Brucher, M., Perrot, M., & Duchesnay, E., 2011. Scikit-learn: Machine learning in python, *Journal of Machine Learning Research*, **12**, 2825–2830.

Rasmussen, C. E. & Williams, C. K., 2006. *Gaussian Processes for Machine learning*, MIT Press, Massachusetts, USA.

Sainburg, T., McInnes, L., & Gentner, T. Q., 2021. Parametric umap embeddings for representation and semisupervised learning, *Neural Computation*, **33**(11), 2881–2907.

Sanvitale, N., Gheller, C., Vazza, F., Bonafede, A., Cuciti, V., De Rubeis, E., Govoni, F., Murgia, M., & Vacca, V., 2025. Mapping diffuse radio sources using tuna: a transformer-based deep learning approach, *MNRAS*, **541**(4), 3479–3493.

Tan, M. & Le, Q. V., 2020. Efficientnet: Rethinking model scaling for convolutional neural networks.

van der Walt, S., Schönberger, J. L., Nunez-Iglesias, J., Boulogne, F., Warner, J. D., Yager, N., Gouillart, E., Yu, T., & the scikit-image contributors, 2014. scikit-image: image processing in python, *PeerJ*, **2**, e453.

van Weeren, R. J., de Gasperin, F., Akamatsu, H., Brüggen, M., Feretti, L., Kang, H., Stroe, A., & Zandanel, F., 2019. Diffuse radio emission from galaxy clusters, *Space Science Reviews*, **215**(1), 16.

van Weeren, R. J., Shimwell, T. W., Botteon, A., Brunetti, G., Brüggen, M., Boxelaar, J. M., Cassano, R., Di Gennaro, G., Andrade-Santos, F., Bonnassieux, E., Bonafede, A., Cuciti, V., Dallacasa, D., de Gasperin, F., Gastaldello, F., Hardcastle, M. J., Hoeft, M., Kraft, R. P., Mandal, S., Rossetti, M., Röttgering, H. J. A., Tasse, C., & Wilber, A. G., 2021. LOFAR observations of galaxy clusters in HETDEX. Extraction and self-calibration of individual LOFAR targets, *A&A*, **651**, A115.

Venturi, T., Giacintucci, S., Merlini, P., Bardelli, S., Busarello, G., Dallacasa, D., Sikhosana, S. P., Marvil, J., Smirnov, O., Bourdin, H., Mazzotta, P., Rossetti, M., Rudnick, L., Bernardi, G., Brüggen, M., Carretti, E., Cassano, R., Di Gennaro, G., Gastaldello, F., Kale, R., Knowles, K., Koribalski, B. S., Heywood, I., Hopkins, A. M., Norris, R. P., Reiprich, T. H., Tasse, C., Vernstrom, T., Zucca, E., Bester, L. H., Diego, J. M.,

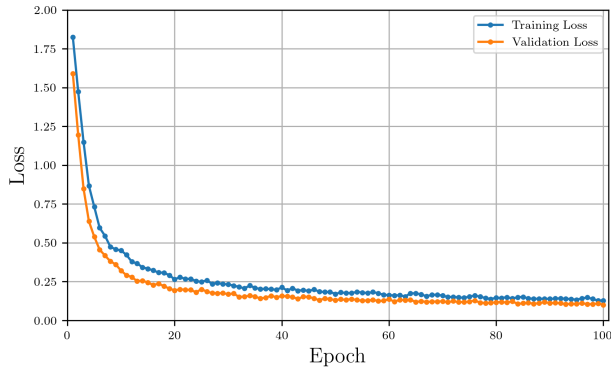


Figure A1. Training and validation loss curves for the BYOL model. The validation set was kept aside to monitor generalisation performance. The alignment of the two curves indicates effective representation learning without overfitting.

& Kanapathippillai, J., 2022. Radio footprints of a minor merger in the Shapley Supercluster: From supercluster down to galactic scales, *A&A*, **660**, A81.

Walmsley, M., Scaife, A. M. M., Lintott, C., Lochner, M., Etsebeth, V., Géron, T., Dickinson, H., Fortson, L., Kruk, S., Masters, K. L., Mantha, K. B., & Simmons, B. D., 2022. Practical galaxy morphology tools from deep supervised representation learning, *MNRAS*, **513**(2), 1581–1599.

APPENDIX A: ADDITIONAL MATERIAL

A1 Model Validation and Loss Curves

During training, a subset of the data was reserved as a validation set for BYOL to monitor generalisation performance. Figure A1 shows that both the training and validation loss decrease steadily and converge, confirming that the model learns robust representations from the data without overfitting.

A2 Illustration of Algorithm Improvement

Figure A2 illustrates the evolution of the active learning process, analogous to Figure 8 in (Lochner & Rudnick 2024). The first row shows the initial random sample, while subsequent rows show the top-ranked sources after each labelling iteration. As the algorithm receives more feedback, it learns to identify and prioritise diffuse emission sources more effectively, as evidenced by the increasing prevalence of interesting sources in the top-ranked positions.

This paper has been typeset from a $\text{\TeX}/\text{\LaTeX}$ file prepared by the author.

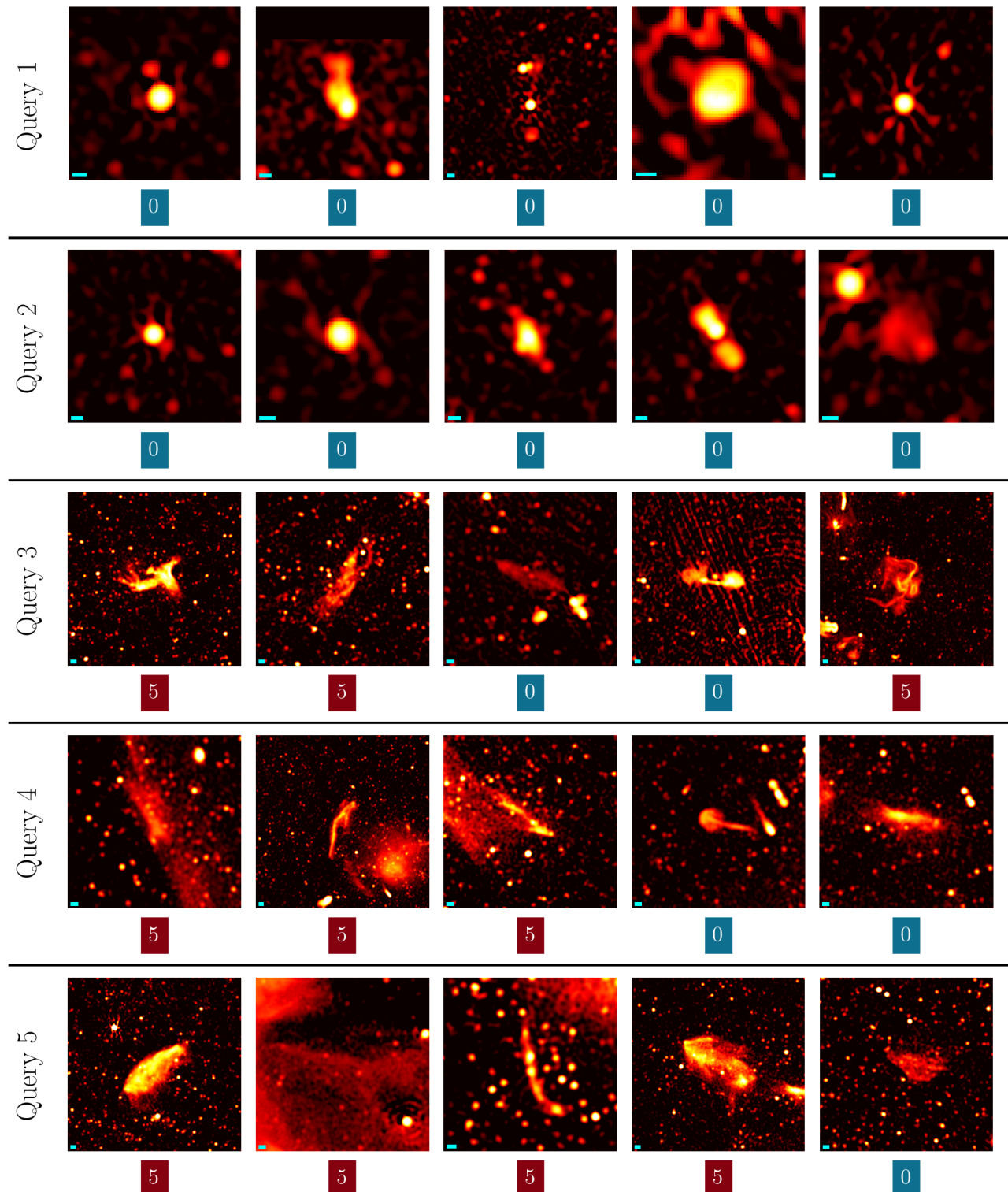


Figure A2. Top 5 sources returned for successive queries during active learning. Each row corresponds to one query iteration, with labels (scores) shown below each source. Over time, more interesting sources are identified and appear earlier in the ranked results, illustrating the effectiveness of the active learning strategy.